remote sensing

MDPI

Article

Features of the Extreme Fire Season of 2021 in Yakutia (Eastern Siberia) and Heavy Air Pollution Caused by Biomass Burning

Oleg Tomshin * and Vladimir Solovyev

Yu.G. Shafer Institute of Cosmophysical Research and Aeronomy of Siberian Branch of the Russian Academy of Sciences, Yakutsk 677027, Russia

* Correspondence: otomshin@ikfia.ysn.ru

Abstract: Yakutia (Eastern Siberia) is one of the most fire-prone regions of Russia, which is frequently affected by large-scale wildfires despite a relatively short warm period, which usually lasts from May to September. In 2021, Yakutia experienced the worst fire season over the last four decades. In this study, we investigate features of the extreme fire season, factors that promote extreme fire weather, and heavy air pollution caused by biomass burning in the region utilizing multiple satellite and ground-based observations along with reanalysis data and forward-trajectory modelling. The results demonstrate that the total number of hotspots (HS) in 2021 amounted to ~150,000, which is almost twice as much as the previous record year (2020). One of the main features of the 2021 fire season was the period of extensive growth of the number of HS, which occurred from 24 July to 12 August. High fire danger during the fire season was promoted by positive anomalies in monthly air temperature (August) and negative anomalies in monthly precipitation (May–July). August of 2021 in central Yakutia was the second most hot August (14.9 °C) during a 43-year NCEP-DOE Reanalysis record (1979–2021). In addition, the intensification of wildfires during August 2021 was associated with persistent high-pressure systems, which promoted dry weather conditions in the region by blocking the transport of moist air masses from the western part of Russia. The low wind speeds, observed in the center of a high-pressure system, led to the accumulation of wildfire emissions in the atmosphere, which significantly affect air quality in the region. The monthly mean aerosol optical depth values in July 2021 were 0.82 (MODIS MAIAC) and 1.37 (AERONET) which were 14.9 and 18.7 times higher than respective values of 2007 (the year with minimal wildfires in the Asian part of Russia and Yakutia). Based on aerosol index observations and forward trajectories, we demonstrate that smoke plumes originated from the study area were transported over long distances reaching the Ural Mountains in the west, Mongolia in the south, the North Pole in the north, and Alaska in the east, traveling the distances of ~2000–7000 km. Maximum spatial extent of the smoke plumes reached ~10–12 mln. km^2.

Keywords: wildfires; fire weather; air quality; air pollution; Siberia; Yakutia

Citation: Tomshin, O.; Solovyev, V. Features of the Extreme Fire Season of 2021 in Yakutia (Eastern Siberia) and Heavy Air Pollution Caused by Biomass Burning. *Remote Sens.* **2022**, *14*, 4980. https://doi.org/10.3390/rs14194980

Academic Editor: Eleni Marinou

Received: 2 September 2022
Accepted: 6 October 2022
Published: 7 October 2022

1. Introduction

Wildfires are a natural disturbing agent in boreal forests which affects carbon cycle and landscape dynamics [1–3]. Despite relatively small annual burned area (~8 Mha/year), boreal fires annually emit ~140 Tg C, which represents 7.0% of the global carbon emissions from fires [4]. Emissions from wildfires, including vast amounts of reflective and absorptive aerosols, significantly affect the air quality and radiative characteristics of the climatic system [5–8]. In Russia, wildfires are the largest source of black carbon (BC) emissions with annual estimates of 569 Gg which is 80% of the country's total BC emissions [9]. Emissions from Siberian wildfires are often transported by air masses over long distances [10–13]. Sources of BC in Siberia, including wildfires, are the major contributors (70%) of near-surface atmospheric BC mass concentration in the Arctic [14]. In addition, fires in the boreal zone can be a significant driver of permafrost degradation, altering the availability of soil

carbon and nutrients that have important implications for future climate and ecological succession [15,16]. With increasing rates of global warming in the Arctic, known as Arctic Amplification [17], it is expected that in nearest future the extent, area, and severity of wildfires will increase [18–20].

In Yakutia (Eastern Siberia) only 2% of the largest fires (>10^4 ha) are responsible for about 75% of the total burned area (BA) while the duration of such catastrophic fires spans from several weeks to months [21]. The emergence of catastrophic large-scale wildfires is often associated with extensive periods of drought and anomalous high air temperatures which are promoted by persistent atmospheric blocking events [22,23]. Several studies have analyzed the connection between circulation patterns and extensive wildfires across the boreal region including Siberia, Alaska, and Canada [24–29].

Larch-dominated boreal forests of Yakutia are one of the most fire-prone regions of Northern Eurasia [3,21,30]. The 2021 fire season was especially extreme, according to the national aerial forest protection service «Aviolesookhrana», the total burned area amounted to 9.4 mln. ha (https://public.aviales.ru/main_pages/openform1.shtml?2021-12-31, accessed on 1 September 2021), which is the largest burned area recorded in the region in almost four decades of satellite observations [30]. Several studies analyzed the causes and consequences of the extreme fire season of 2021 in Yakutia. Hayasaka [26] made a detailed analysis of atmospheric conditions during the fire season. He found that the main drivers of extreme fire weather in the region were the large meandering westerlies, which brought high-pressure systems and warm air masses from the south, and strong southeasterly winds at lower air levels, which were related to the development of high-pressure systems in the Arctic Ocean. Ponomarev et al. [31] estimated the total area of stand-replacement fires at ~2.5 mil. ha in 2021 in Yakutia. Stand-replacing fires are characterized by significant tree mortality and lead to the initiation of a succession or regrowth [32,33]. Such high-intensity fires are also release greater amounts of combustion products into the atmosphere [34].

This study aims to investigate features of the extreme fire season of 2021 in Yakutia, factors that promote extreme fire weather, and its impact on air pollution in the region. To do that we (1) describe spatio-temporal patterns of wildfires; (2) analyze daily and monthly weather conditions, which promoted the large-scale forest fires; (3) examine the properties of aerosols emitted from wildfires, their seasonal and vertical distribution as well as long-range transport.

2. Materials and Methods

2.1. Study Area

Yakutia is a republic within the Russian Federation, located in Eastern Siberia with an area of over 3 mil. km^2, completely underlined by permafrost, and with a population of about 1 mil. people (Figure 1b). The climate of the region is sharply continental with an annual temperature range of ~100 °C: from −70 °C in winter to 40 °C in summer. The annual amount of precipitation is low (~250–300 mm) with frequent droughts. As a result of climate change during the last 50 years, air temperature in Yakutia has risen up to 3 °C [35].

The territory of Yakutia is characterized by arctic (26%) and boreal (74%) vegetation communities. Arctic vegetation dominates the region's high latitudes along the coast of the Arctic Ocean, while boreal forests cover the rest of the region. The boreal group is prevailed by the taiga type with common light coniferous larch forests [36].

Despite the relatively short warm period, which usually lasts from May to September, Yakutia is frequently affected by large-scale wildfires [10,21,26,37]. This is the result of the combination of favorable climatic and weather conditions, along with vast hard-to-reach forested territories and low population density. The most frequently burned territories over the past few decades are located in central Yakutia (Figure 1a, dashed rectangle): Lena-Vilyui interfluves and the left bank of the Aldan River. Major wildfires in 2021 were also located in this region and we defined it as our study area with the following boundaries: 110–140°E, 60–67°N.

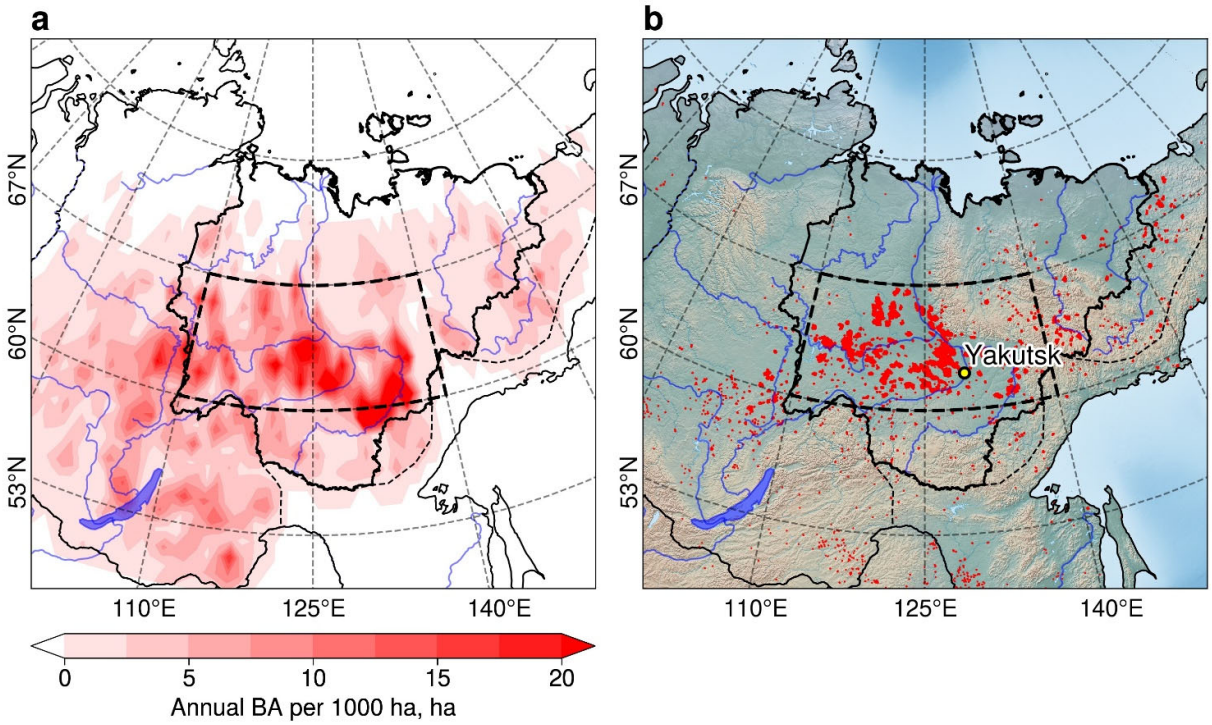

Figure 1. (**a**) Annual mean burned area per 1000 ha in Eastern Siberia during 1984–2016 obtained from ES-BA dataset [30]; (**b**) MODIS hotspots detected during 2021 (red dots). Bold black line—Yakutia, bold dashed black rectangle—study region, thin dashed line—Eastern Siberia, blue lines—rivers.

2.2. Data

2.2.1. MODIS Active Fire Product

Spatial and temporal dynamics of wildfires were analyzed using thermal anomalies or hotspots (HS) obtained from the Moderate Resolution Imaging Spectroradiometer (MODIS) MCD14ML C6 product [38]. MODIS active fire algorithm uses brightness temperatures to identify "fire pixels" that contain one or more actively burning fires at the time of the satellite overpass at a 1 km spatial resolution. Despite low spatial resolution in comparison to other similar products [39], MODIS active fire data is a valuable source of information due to the long operational time spanning the period from 2001 to present. Apart from wildfires, several other sources can produce a similar thermal signal which can lead to false positive detections, in particular gas flares [40], which are widespread in the southern part of Yakutia. We excluded gas flare detections from MODIS data by applying a simple spatial mask around mineral extraction areas identified from higher-resolution imagery. Additionally, to limit multiple detections of thermal anomalies produced by the same wildfires we used MODIS data obtained only by the Terra satellite. HS with nominal and high confidence defined by MODIS active fire algorithm were used in this study. MODIS active fire data were obtained from The Fire Information for Resource Management System (FIRMS, https://firms.modaps.eosdis.nasa.gov/, accessed on 20 June 2022).

2.2.2. MODIS Aerosol Products

Data on aerosol optical depth (AOD) at 550 nm were obtained from several MODIS products generated with different algorithms. Currently, there are several operational MODIS AOD algorithms: the Dark Target (DT) algorithm over land and ocean [41], the Deep Blue (DB) algorithm [42], and the Multi-Angle Implementation of Atmospheric Correction (MAIAC) algorithm [43]. The DT algorithm uses a set of ratios and relationships between the 470, 670, and 2100 nm channels to account for the surface signal and works best over dark vegetated targets while does not work over bright land surfaces. The DB algorithm uses surface reflectance in the blue channels to account for the surface signal and

works best over bright land surfaces but can also retrieve aerosols over most vegetated targets. Additionally, the DT and DB algorithms outputs are used to generate a combined DT and DB (DTDB) dataset [41] to improve data coverage and leverage the strengths of the two aerosol retrieval algorithms. MAIAC algorithm uses time series analysis and a combination of pixel- and image-based processing to improve the accuracy of cloud detection, aerosol retrievals, and atmospheric correction. The algorithm shows good performance for both dark and bright surfaces.

In this study, we used AOD data from a combined DTDB dataset (product MOD04_L2 C6.1) and MAIAC (product MCD19A2 C6). MOD04_L2 is a Level 2 aerosol product generated from Terra observations with 10 km spatial resolution. MCD19A2 C6 is a daily Level 2 product with a 1 km spatial resolution produced both from Terra and Aqua observations. MODIS data from both algorithms was filtered using quality control flags to include only the best measurements. MODIS aerosol products were obtained from NASA's Earth Observing System Data and Information System (EOSDIS, https://www.earthdata.nasa.gov/, accessed on 10 June 2022).

2.2.3. AERONET Aerosol Optical Depth

AERONET (AErosol RObotic NETwork) is a global aerosol monitoring network based on ground-based sun-sky photometers [44]. AERONET provides globally distributed observations of aerosol microphysical, optical and radiative properties. In this study, we used level 2.0 quality-assured and cloud-cleared data on AOD at 500 nm obtained at Yakutsk station (Figure 1b) by CIMEL CE-318 sun photometer. The data was produced by the AERONET version 3 retrieval algorithm, which is based on the Version 2 algorithm with numerous updates [45]. The data was downloaded from the AERONET website (https://aeronet.gsfc.nasa.gov/, accessed on 19 July 2022).

2.2.4. OMPS-NM Aerosol Index Product

As an additional source of information on aerosol loading, we used UV-absorbing Aerosol Index (AI) observations from Ozone Mapping and Profiler Suite Nadir Mapper (OMPS-NM) aboard the Suomi-NPP satellite (product NMMIEAI-L2). AI is based on a spectral contrast method in a UV region where the ozone absorption is very small (340–379 nm). A positive AI value indicates the presence of UV-absorbing aerosols such as smoke or dust. The NMMIEAI-L2 is a daily Level 2 product with a nadir pixel size of 50×50 km. Daily AI values over the study area were derived as the mean of all Level 2 pixels with AI ≥ 0.5, to exclude AI values associated with clouds or reflective aerosols. OMPS-NM data was obtained from NASA's Earth Observing System Data and Information System (EOSDIS, https://www.earthdata.nasa.gov/, accessed on 10 June 2022).

2.2.5. CALIOP Aerosol Profile Product

The Cloud-Aerosol LIdar with Orthogonal Polarization (CALIOP) onboard NASA CALIPSO satellite provides near-nadir aerosol properties at 532 and 1064 nm [46]. Lidar technique allows obtaining high-resolution vertical profiles of aerosols and is capable to observe aerosols above bright surfaces including clouds, snow, and deserts. CALIOP is capable to classify 7 tropospheric aerosol types based on measurements of depolarization ratio [47]: clean marine, dust, polluted continental and elevated smoke, clean continental, polluted dust, elevated smoke, and dusty marine. In present study, we used monthly Level 3 tropospheric aerosol profile product v. 4.21 to identify aerosol types over the study region including both day and night cloud-free CALIOP measurements. We calculated occurrence frequency (OF) of each aerosol type by dividing the number of observations or samples of specific type by the total number of CALIOP samples in a given month over the study region including both aerosol and clear air samples. CALIOP data were obtained from NASA Atmospheric Science Data Center (ASDC, https://asdc.larc.nasa.gov/, accessed on 27 April 2022).

2.2.6. AIRS Carbon Monoxide Product

Since carbon monoxide can persist for a long time in the atmosphere (~1 month), we use it to trace the pathways of the long-range transport of wildfire emissions. We used Atmospheric Infrared Sounder (AIRS) data to analyze spatio-temporal patterns of carbon monoxide during the 2021 fire season in Yakutia. AIRS is a thermal hyperspectral sensor with more than 2000 channels installed aboard NASA's Aqua satellite with low, sun-synchronous orbit. The AIRS Level 3 product (AIRS3STD C6) contains daily quality-controlled information on carbon monoxide concentration at 500 hPa pressure level (~5500 m) at 1° spatial resolution [48]. AIRS data was obtained from NASA's Earth Observing System Data and Information System (EOSDIS, https://www.earthdata.nasa.gov/, accessed on 10 June 2022).

2.2.7. Meteorological Data

In this study we considered several weather parameters related either to upper or surface level weather conditions, which were shown to be sensitive to fire weather in the boreal region [25]. For upper-level conditions, we analyzed geopotential height at 500 hPa (Z500) and wind speed and direction at 300 and 850 hPa. For surface-level—air temperature at 2 m (T2m), precipitation (P), and sea level pressure (SLP). We derived daily fields of Z500, winds, T2m, and SLP from NCEP–DOE II Reanalysis [49] defined either on a regular 2.5° × 2.5° or on a spectral Gaussian grid.

Daily and monthly precipitation values were obtained from the Global Precipitation Climatology Centre (GPCC). GPCC global land-surface precipitation products are based on rain gauge data reported in near-real time via the Global Telecommunication System of the World Meteorological Organization. We used first guess daily and first guess monthly products with 1° spatial resolution [50].

To compute anomalies, we calculated climatologies of each parameter using daily data from 1980 to 2010 for fields obtained from NCEP–DOE II Reanalysis (Z500, SLP, T2m). For precipitation data, we used precipitation climatology (1951–2000) obtained from GPCC [51].

2.2.8. HYSPLIT Forward Trajectories

The HYbrid Single-Particle Lagrangian Integrated Trajectory (HYSPLIT) model developed by the National Oceanic and Atmospheric Administration Air Resources Laboratory [52] was used to compute forward trajectories of air masses to track the movement of smoke plumes originated from the wildfires in the study region. NCEP/NCAR Reanalysis data was used as input to calculate 7 and 14-day trajectories originating from 36 starting locations evenly spaced over the study region (1.4° × 6° lat/lon) from 3000 m and 5000 m altitudes at 6-hour intervals.

3. Results

3.1. Features of the 2021 Fire Season

The 2021 fire season in Yakutia was the most catastrophic and unprecedented in nearly four decades of satellite observations of wildfires in the region [30]. The daily number of hotspots during 2001–2021 fire seasons is presented as a cumulative total in Figure 2a and monthly number of HS can be seen on Figure 2b. We averaged the number of HS during the years with low (2003–2011, 2015–2017) and moderate (2001, 2012–2014, 2018–2019) wildfire activity, and 2002, 2020, and 2021, the most extreme years, are shown separately. As can be seen from the figure, the number of HS in Yakutia usually starts to rise in the second part of June, followed by uniform growth in July. During the years with low and moderate wildfire activity, the growth of HS in August is very limited, in contrast to the most extreme fire seasons (2002, 2020, 2021), when HS continues to grow till the second half of August (2002) or even later (2020, 2021). Another important feature of the 2020 and 2021 fire seasons is an earlier start of the extensive growth of HS, which occurred at the beginning of July with doubled amount of HS compared to other years.

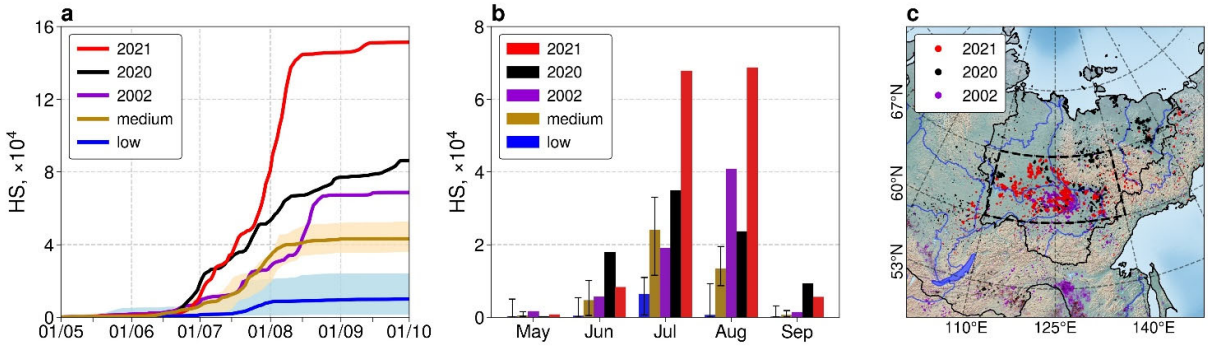

Figure 2. (**a**) Number of daily HS in Yakutia as a cumulative total; (**b**) monthly number of HS in Yakutia; (**c**) Map of HS in 2002 (purple), 2020 (black), and 2021 (red). Blue line (**a**) and bars (**b**)—median values during years with low wildfire activity (2003–2011, 2015–2017), orange line (**a**) and bars (**b**)—median values during years with moderate wildfire activity (2001, 2012–2014, 2018–2019). Shaded areas (**a**) and whiskers (**b**) indicate a 5–95 percentile range.

The total number of hotspots in 2021 amounted to ~150,000, followed by 2020 (~86,000) and 2002 (~68,000). For comparison, the total number of HS in years with low wildfire activity is usually in the range of 100−24,000, and in years with moderate wildfire activity is 36,000−52,000. The main difference between the 2021 fire season and other extreme seasons (2002, 2020) is the period of extensive growth of the number of HS, which occurred in the period from 24 July to 12 August. During this 20-day period, the total number of HS almost tripled from 49,000 to 140,000. A somewhat similar rapid growth of HS was also observed during 2002, when in the 12-day period from 12 August to 24 August total number of HS increased from 35,000 to 66,000. Such rapid growth of HS is directly linked to the expansion of the area of wildfires as HS are typically observed at a fire front.

The majority of wildfires during the 2021 fire season were located in the central part of Yakutia (Figure 2c). The same spatial distribution was observed in 2002 while in 2020 a significant part of wildfires occurred in the northeastern part of Yakutia, beyond the Arctic Circle. A thorough analysis of the spatial distribution of HS in those three extreme seasons showed, that areas affected by wildfires in 2002 and 2021 are weakly overlapped despite an almost 20-year gap between these seasons.

3.2. Weather Conditions during the 2021 Fire Season

3.2.1. Daily and Monthly Variations of HS, Air Temperature, and Precipitation

To describe surface-level weather conditions during the fire season we analyzed daily and monthly variations of HS, air temperature, and precipitation (Figure 3). The 2021 fire season is characterized by two distinct periods of wildfire activity: first—from late June to 23 July and second (main) from 24 July to 17 August (Figure 3a). The maximum daily number of HS during the first period was 3313 (8 July), and during the second—8680 (2 August). This corresponds to the typical season course of wildfires in the region—usually, fire season starts in May, followed by intensification of wildfires in July, as air temperature rises, then maximum in late July–August and end of a fire season in September [53].

In 2021, variations of daily air temperature anomalies during the earlier part of the fire season (May–June) and the first active period were mainly short-term: the duration of positive anomalies typically lasted from 2–5 days after which they were replaced by negative anomalies (Figure 3c). From 19 July till 26 August the positive temperature anomalies prevail in the region, with the maximum daily value reaching +5.6 °C, while the average value during the period was +2.8 ± 1.6 °C. The correlation between daily air temperature and the number of HS during the two periods was $r = 0.41$.

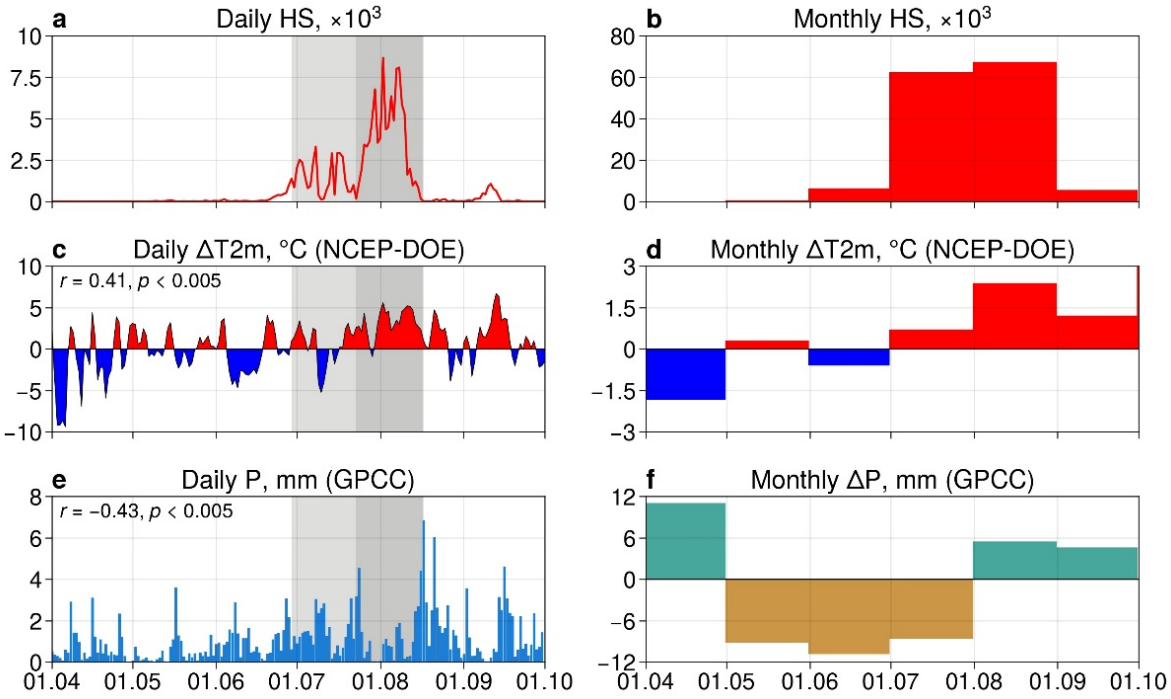

Figure 3. (**a**) Daily and (**b**) monthly number of HS; (**c**) daily and (**d**) monthly anomalies of air temperature; (**e**) daily total and (**f**) monthly anomalies of precipitation. Grey vertical bars indicate two periods of wildfire activity. All data correspond to the study region. Correlation coefficients on figures (**c**,**e**) indicate correlation between the number of HS and the corresponding parameter during the period from 29 June to 17 August.

The same behavior is observed on a monthly scale (Figure 3d): during May and June air temperatures are closer to a long-term mean (+0.3 °C and −0.6 °C, respectively), which is then followed by an increase in July (+0.7 °C), August (+2.4 °C) and September (+1.2 °C). According to the monthly average air temperature, August of 2021 in central Yakutia was the second most hot August (14.9 °C) during a 43-year NCEP-DOE Reanalysis record (1979–2021), second only to August of 2017 (15.0 °C) and followed by August 2002 (14.8 °C), while average august temperature in the region is 12.8 ± 1.4 °C.

Annual precipitation in Yakutia is generally low (250–300 mm) due to the sharply continental climate of the region. The summer of 2021 was one of the driest summers in Central Yakutia in recent history: monthly anomalies of precipitation (Figure 3f) in May, June, and July were −9.1, −10.7, −8.5 mm, while the climatological amount of precipitation for these months are 23.7, 41.9 and 50.7 mm, respectively. The daily amount of precipitation (Figure 3e) during the second period of the intensification of wildfires in the region was 1.4 ± 1.7 mm/day, while generally daily precipitation of less than 5 mm can't significantly affect the spread of a wildfire [54]. Since 13 August, one can observe the increase of daily precipitation in the region with a maximum of 6.9 mm on 17 August. During this period, the amount of HS was significantly reduced to a minimal level. The correlation between daily precipitation and the number of HS during the two periods was $r = -0.43$.

The observed temperature and precipitation anomalies contributed to the development of favorable meteorological conditions for the ignition and spread of wildfires in the region.

3.2.2. Synoptic-Scale Weather Conditions during the Main Active Fire Period

Significant positive anomalies of air temperature and a low amount of precipitation during the main period of wildfire intensification in the region were promoted by persistent high-pressure systems [26]. To characterize spatio-temporal patterns of high-pressure systems we use daily anomalies of geopotential height at 500 hPa (ΔZ500) with 300 hPa winds and sea-level pressure maps (ΔSLP) combined with 850 hPa winds. According

to ΔSLP and ΔZ500 values (Figure 4e,f), the study region was under the influence of anticyclonic circulation from late July to the middle of August with maximum observed on 31 July in ΔSLP values (+8.8 mbar) and on 1 August in ΔZ500 values (+182 m). ΔSLP values show a higher correlation (r = 0.62) with the number of HS than ΔZ500 values (r = 0.52). As can be seen from Figure 4a,b, high-pressure anomalies on 31 July covered a major part of Eastern Siberia with maximum located over central and northern Yakutia. In the same area, one can observe a cloudless (Figure 4d) region of high positive air temperature anomalies at 2 m with maximum values located in northern Yakutia (+9.8 °C). Observed during the main fire period high-pressure systems promoted dry weather conditions in the region by blocking the transport of moist air masses from the western part of Russia. During the anticyclone's maximum (30 July–1 August), almost no precipitation was observed over the entire study region (Figure 3e). Low wind speeds, observed in the center of a high-pressure system, led to the accumulation of biomass burning emissions in the atmosphere, which significantly affect air quality in the region.

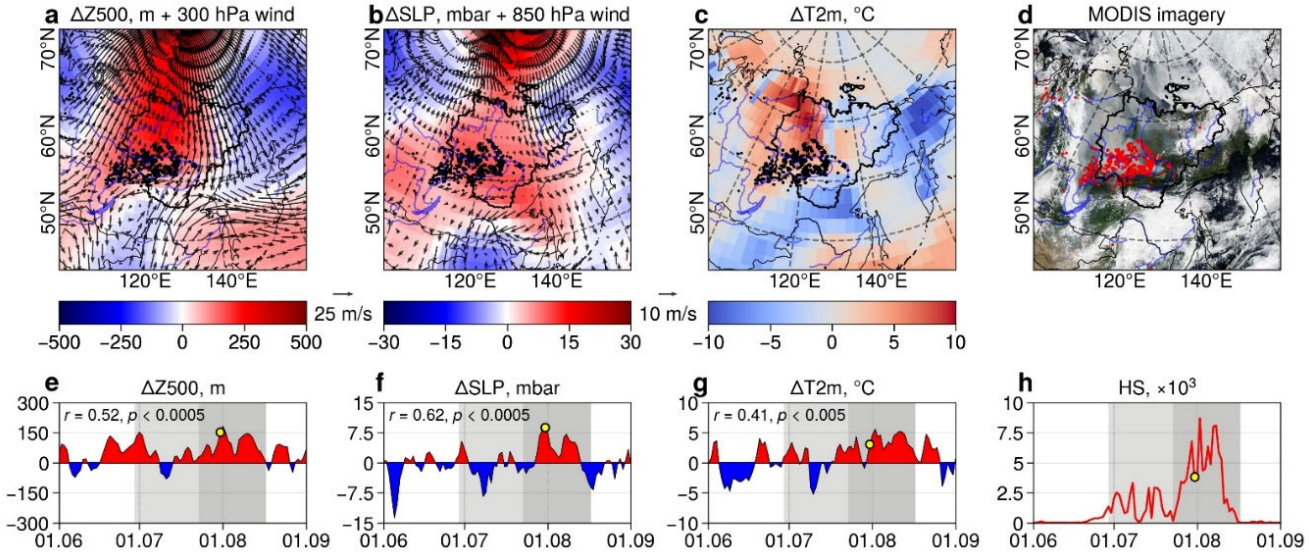

Figure 4. (**a**,**e**) Geopotential height anomalies at 500 hPa (ΔZ500) and vector wind field at 300 hPa; (**b**,**f**) sea level pressure anomalies (ΔSLP) and vector wind field at 10 m; (**c**,**g**) air temperature anomalies at 2 m (ΔT2m); (**d**) MODIS imagery; (**h**) MODIS hotspots. Figures (**a**–**d**) show weather conditions on 31 July 2021; black (**a**–**c**) and red (**d**) dots are MODIS HS. Line plots (**e**–**h**) refer to the study region, the yellow markers indicate 31 July. Grey vertical bars indicate two periods of wildfire activity. Correlation coefficients on figures (**e**–**g**) indicate correlation between the number of HS and the corresponding parameter during the period from 29 June to 17 August.

3.3. Spatio-Temporal Variations of Aerosol Parameters

3.3.1. Daily and Monthly AOD

To characterize aerosol loading over the study region during 2021 we use daily AOD and AI observations. Daily values of AOD (Figure 5b–d) over the study region were highly variable during the summer. All products report an increase in AOD since the beginning of the wildfires at the end of June with no significant differences in AOD values between the first and second fire periods and an abrupt decrease in the middle of August due to rainfalls (Figure 3e). Among the three examined AOD products, the lowest absolute values were reported by MODIS combined DTDB algorithm, followed by AOD observations from the MODIS MAIAC product and the AERONET sun photometer, which reported the highest values. Maximum area-averaged daily values of AOD: during the first period—1.7 (DTDB), 2.1 (MAIAC), 3.7 (AERONET); during the second period—1.4 (DTDB), 2.2 (MAIAC), 3.1 (AERONET). The highest correlation with the number of HS is observed in AI values (r = 0.73), and the lowest is in AERONET AOD (r = 0.25). The low correlation

between AERONET AOD and HS is because AERONET data is representing AOD values at a single station while satellite-based AOD are area averages and thus had better reflect AOD variations over the study region. A higher correlation between HS and AI values in comparison to AOD is due to AI's ability to better identify aerosol plumes in difficult conditions (e.g., clouds and other bright surfaces).

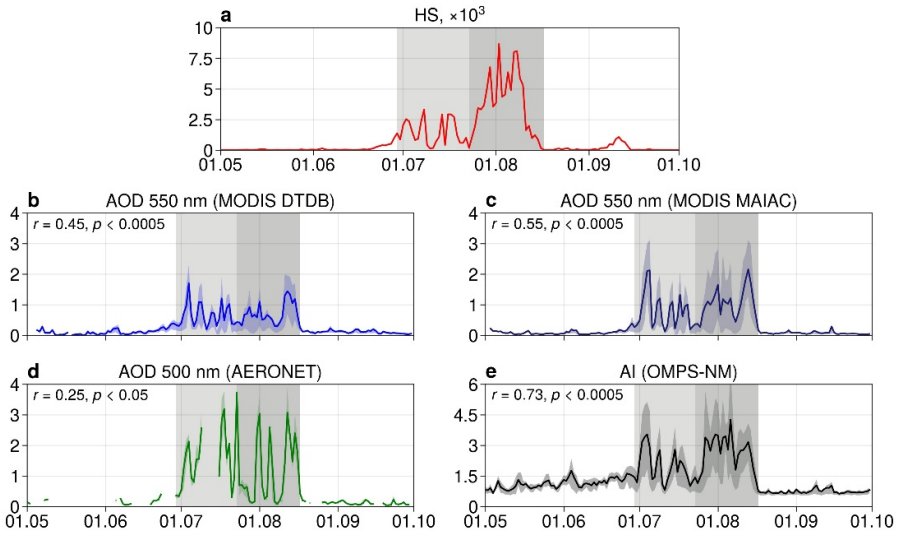

Figure 5. (**a**) MODIS hotspots; (**b**) AOD at 550 nm from MODIS DTDB algorithm; (**c**) AOD at 550 nm from MODIS MAIAC algorithm; (**d**) AOD at 500 nm from AERONET sun photometer at Yakutsk; (**e**) aerosol index from OMPS-NM. Grey vertical bars indicate two periods of wildfire activity. Shaded areas on figures (**b**–**e**) indicate a 25–75 percentile range. Figures (**b**,**c**,**e**) represent mean values over the study region. Correlation coefficients on figures (**b**–**e**) indicate correlation between the number of HS and the corresponding parameter during the period from 1 May to 30 September.

During the second fire period, most of the region was experiencing heavy air pollution due to a combination of extensive wildfires and a high-pressure system. Figure 6c,d are pictures taken at the towns of Vilyuysk and Nyurba on 2 August at approximately 19:25 and 20:55 local time. According to MODIS HS (Figure 6a), the towns were between several major wildfires, at the center of the high-pressure system (Figure 4b) characterized by low surface wind speeds, which promoted the accumulation of aerosol emissions in the atmosphere. OMPS-NM aerosol index map for the date (Figure 6b) shows that most of the western part of Eastern Siberia was covered by areas with AI values ≥ 3, indicating a high concentration of aerosol particles. This led to an extreme air pollution episode that resulted in the orange and red colored skies as seen from the ground due to Mie scattering. A complete blackout during the daytime was also reported in several settlements in the affected area during the second fire period.

Monthly AOD values during 2021 (Figure 7b) demonstrate the same pattern with the lowest AOD values reported by the DTDB algorithm. For comparison, we obtained monthly AOD over the study region during 2007 (Figure 7a). We selected 2007 as it was the year with the lowest burned area in the Asian part of Russia and Yakutia, so one may consider it as a background condition with a minimal influence of biomass burning aerosols. Monthly mean AOD during May–September 2007 is typically lying in the range from 0.05 to 0.15 with slight month-to-month and product-to-product variations. Monthly mean AOD values during July 2021 were 0.66 (DTDB), 0.82 (MAIAC), and 1.37 (AERONET) which were 7.8, 14.9, and 18.7 times higher than the respective values from 2007. August AOD was slightly lower primarily due to rainfalls in the middle of the month: 0.47 (DTDB), 0.64 (MAIAC), and 0.9 (AERONET), which exceed 2007 values by factors of 6.3, 11.9, and 9.9, respectively.

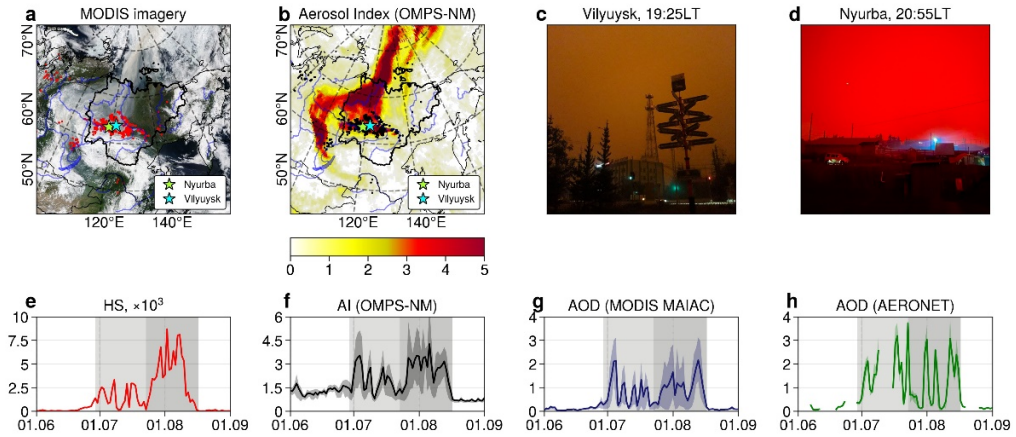

Figure 6. Aerosol pollution episode on 2 August. (**a**) MODIS imagery; (**b**,**f**) aerosol index; (**c**,**d**) pictures of the sky taken at the towns of Vilyuysk and Nyurba at approximately 19:25 LT and 20:55 LT; (**e**) MODIS hotspots; (**g**) AOD at 550 nm from MODIS MAIAC algorithm; (**h**) AOD at 500 nm from AERONET sun photometer at Yakutsk. Red (**a**) and black (**b**) dots are MODIS HS. Star symbols (**a**,**b**) indicate the locations of the settlements. Grey vertical bars indicate two periods of wildfire activity. Line plots (**e**–**h**) refer to the study region. Shaded areas on figures (**f**–**h**) indicate a 25–75 percentile range.

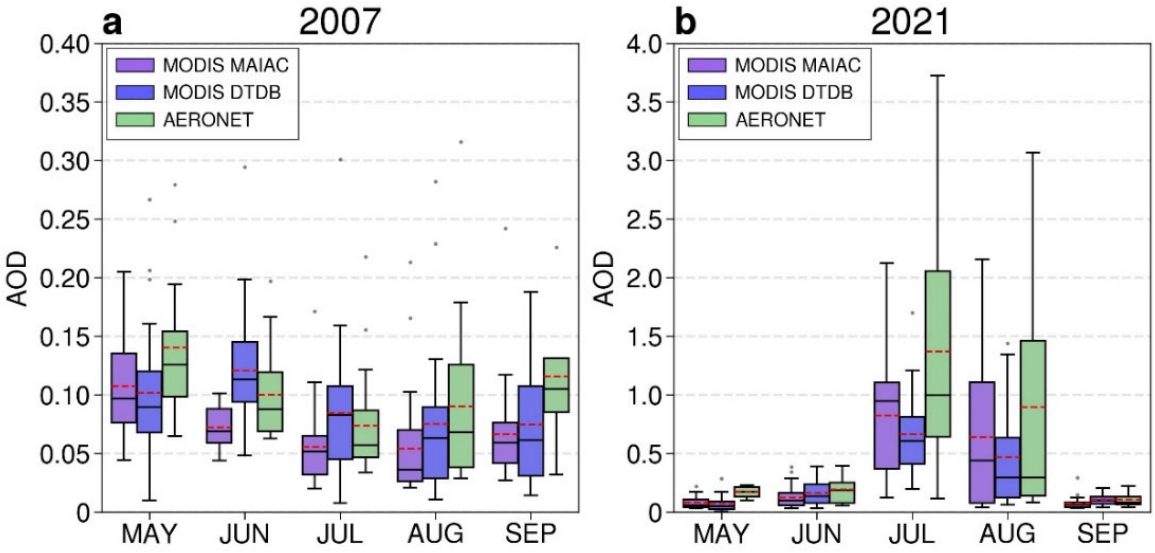

Figure 7. (**a**) Monthly statistics of aerosol optical depth from MODIS DTDB, MAIAC algorithms, and AERONET during 2007; (**b**) same but for 2021. MODIS AOD observations are averaged over the study region from daily data. Dashed red lines indicate the mean value. Note that figures (**a**) and (**b**) use different ranges on the *y*-axes.

MODIS DTDB algorithm tends to report lower values due to a limited ability to correctly discriminate clouds/smoke plumes during major biomass burning episodes [55]. MAIAC on the other hand discriminates smoke from clouds using a relative increase in aerosol absorption at 412 nm compared to 470–670 nm due to multiple scattering and enhanced absorption by organic carbon released during combustion which leads to improved data coverage [56].

3.3.2. Seasonality of Aerosol Types over the Study Region

According to CALIOP data, there are typically five aerosol types, presented over the study region during the year (Figure 8): elevated smoke (ES), polluted dust (PD), clean continental (CC), polluted continental/elevated smoke (PCS) and dust (D). Both polluted

types (PD, PCS) represent a mixture of dust and polluted continental types, respectively, with biomass burning aerosols [47]. Seasonal patterns of all major aerosol types presented over the study region have a distinctive winter-spring peak in 2007—a year with a minimal number of wildfires (Figure 8a). The highest OF during this period belongs to the PD type with a maximum in April, followed by the PCS type with a maximum in March. Distinctive winter peaks in February are also observed in CC, ES, and D types. The lowest OF in all aerosol types in 2007 was observed during summer and early autumn (June–October), except for the PCS type, which has a small peak in August. After October, the OF of most of the types start to rise. Contrary to 2007, in 2021 there are two distinct seasonal peaks in aerosol load (Figure 8b). As in 2007, most of the aerosol types have a peak during the winter-spring months (January–March). The highest OF during this period belong to PD, PCS, and D aerosol types. After the winter peak, the OF of all types is decreasing until it reaches the local minimum in May. Next, CC and D types show negligible variation around minimal values until November-December, while PCS, ES, and PD types start to rise to form the second summer peak in July–August, which is caused by biomass burning in the region. After the end of the fire season in September, the OF in those three types demonstrates a sharp decrease to minimal values in September–October followed by an increase in November–December, as in 2007. As suggested in [57,58], the winter peak in aerosol load is most likely caused by the long-range transport of aerosols from other regions of Siberia.

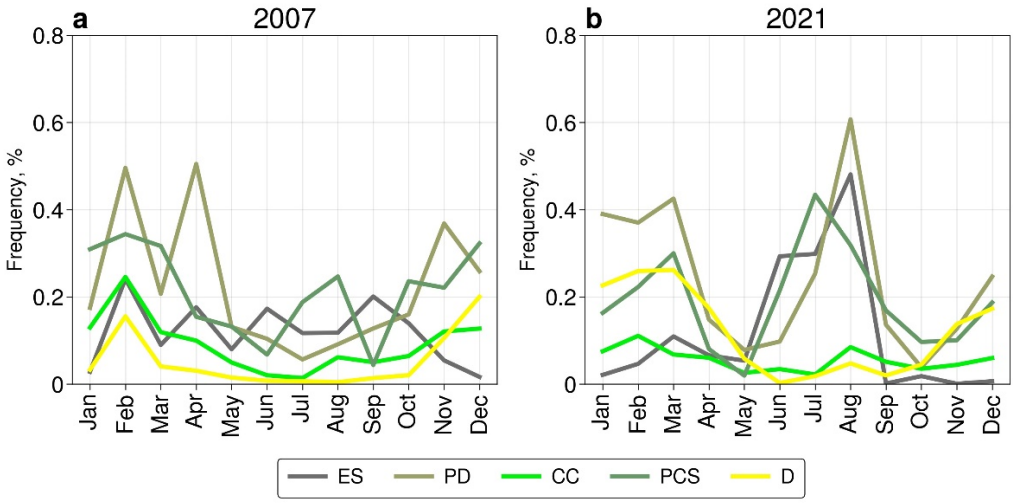

Figure 8. Occurrence frequency of each CALIOP aerosol type for (**a**) 2007 and (**b**) 2021. Aerosol types: ES—elevated smoke, PD—polluted dust, CC—clean continental, PCS—polluted continental/smoke, D—dust.

3.3.3. Vertical Distribution by Aerosol Types

The vertical distribution of OF by aerosol types over the study region during June–August 2007 is presented in Figure 9a–c. In June 2007, most of aerosol layers are registered in the altitude range of 0–5 km. A small number of polluted dust and dust layers are also observed at 8–9 km. In June and August, one can observe a growth in polluted continental/smoke type mainly located at 0.7–2 km altitude range, caused by the small wildfires in the Asian part of Russia. In contrast, in 2021 an increased aerosol load is already observed in June (Figure 9d), mainly formed by ES and PCS types at altitudes of 0.5–4 km. As the number and area of wildfires start to grow in July, the increase of biomass burning related types is observed (Figure 9e): polluted continental/smoke type reaches its maximum at altitudes 0.8–2.5 km; polluted dust type was registered at 0.8–5 km; elevated smoke has a maximum at 5 km, but some layers rise up to 7 km. In August 2021 (Figure 9f) one can observe a sharp increase in aerosol load at high altitudes: elevated smoke type has

a maximum at 3 km with some layers reaching up to 11 km; polluted dust type is presented in large amounts at 0.5–6 km range with an additional peak at 9 km.

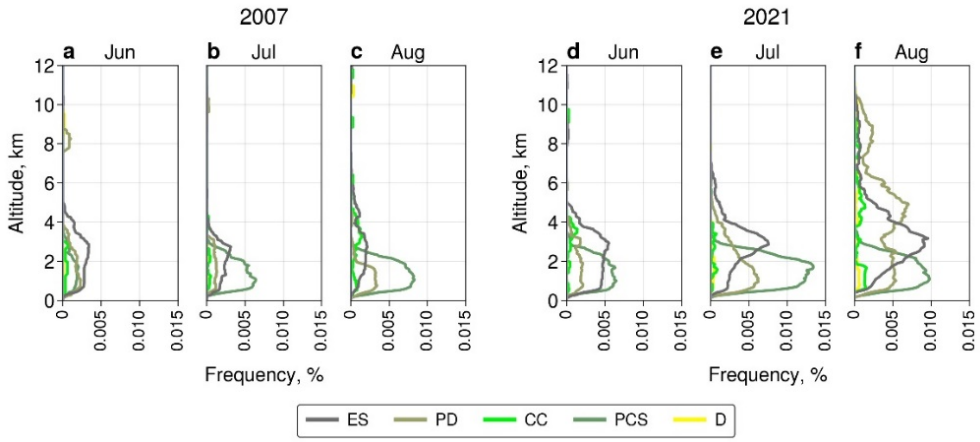

Figure 9. Occurrence frequency profile of each CALIOP aerosol type for (**a**) June, (**b**) July, (**c**) August 2007, and (**d**) June, (**e**) July, and (**f**) August 2021. Aerosol types: ES—elevated smoke, PD—polluted dust, CC—clean continental, PCS—polluted continental/smoke, D—dust.

3.3.4. Long-Range Transport of Air Pollution

In this section, we describe the long-range transport of biomass burning aerosols that originated from central Yakutia during the second period of wildfire intensification by analyzing daily maps of the aerosol index and carbon monoxide along with the HYSPLIT forward trajectories. Figure 10 shows daily maps of the OMPS-NM aerosol index from 26 July to 15 August. During this period, besides large-scale wildfires in the study region (~160,000 HS), wildfires in Siberia were mostly located in the central part of Eastern Siberia (105–109°E, 57–63°N) with ~9700 HS in that area during the period. In the first three days, all smoke plumes were located within the study region, while aerosol index values were already high (≥4). With a growing number of wildfires in the region and change in wind pattern, the aerosol plumes start to expand over larger territories mostly in the northern and north-western direction, towards the Arctic, reaching the North Pole several times during the first eight days of August. From 5 August until 11 August, aerosol plumes were transported in western and south-western directions reaching the Ural Mountains in the west and Mongolia in the south. During this period, the spatial extent of aerosol plumes reached its maximum, covering most of Siberia with an affected area of approximately 10 mil. km^2. Deterioration of air quality at that time was reported in several large cities of Siberia, including Yakutsk (pop. ~0.34 mil.), Irkutsk (pop. ~0.62 mil.), Krasnoyarsk (pop. ~1.1 mil.), and Novosibirsk (pop. ~1.6 mil.). After 11 August, aerosol index values start to decrease as the number of wildfires in the study region also began to decrease. During this period, aerosol plumes were transported in the eastern direction, reaching Alaska and Canada.

The same overall patterns are observed in AIRS carbon monoxide concentration at 500 hPa (Figure 11). As carbon monoxide has a long lifetime in the atmosphere, it can be better traced over long distances from the source. High CO concentration (≥300 ppbv) during the period was observed over most of Siberia. At the end of the period (15 August), in contrast with the aerosol index values, which start to decrease, carbon monoxide concentration remained high over the Sea of Okhotsk, the Bering Sea, and Alaska with an affected area of approximately 12 mil. km^2.

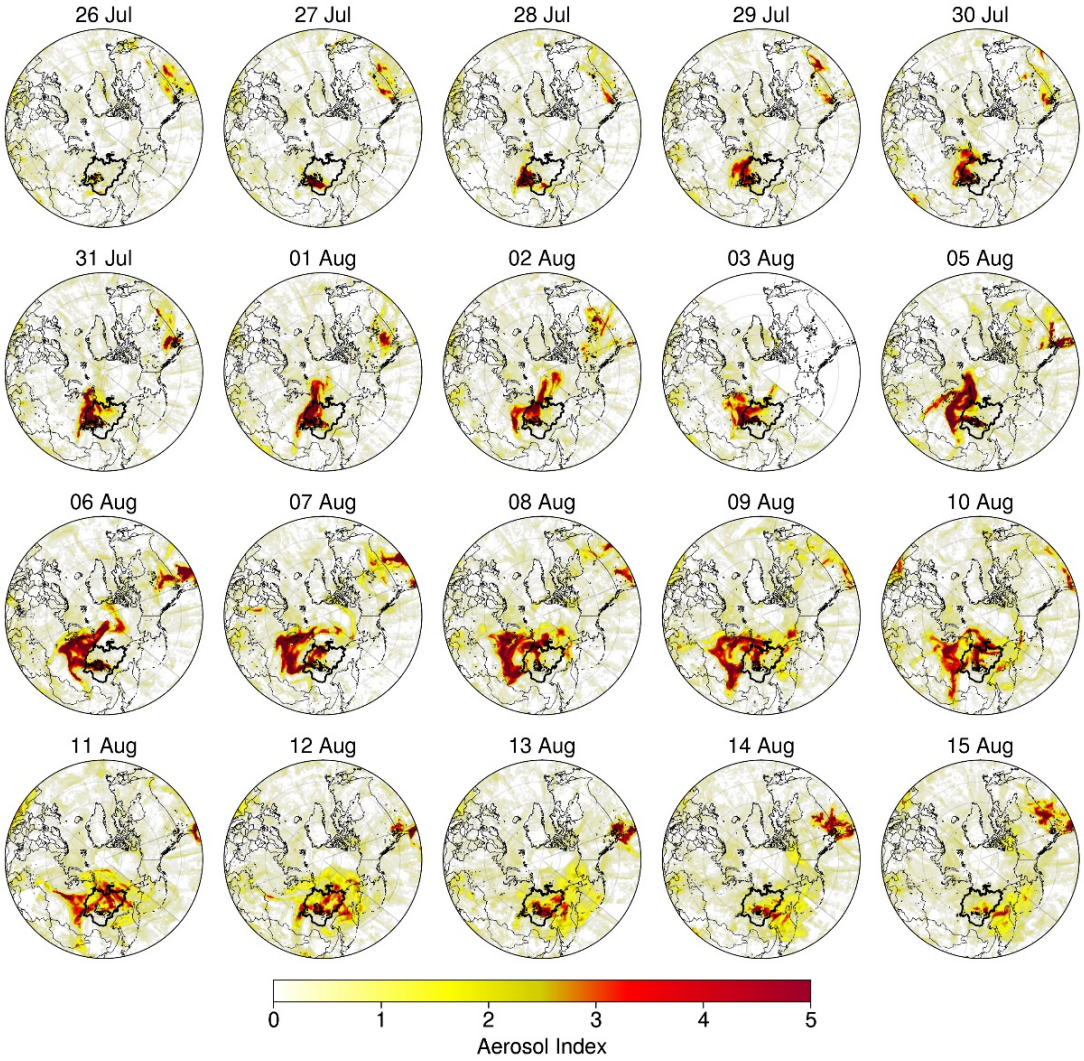

Figure 10. Spatial distribution of OMPS-NM aerosol index during the second period of wildfire intensification in the study region (26 July–15 August). The bold solid line indicates Yakutia administrative boundary, black dots—MODIS hotspots.

To visualize the pathways of aerosol transport from the study region we computed forward trajectories of air masses during the second fire period (26 July–15 August) using the HYSPLIT model (Figure 12). Trajectories' starting altitudes of 3 and 5 km were used as CALIOP aerosol profiles indicated the peaks of biomass burning aerosols at these heights during August (Figure 9f). Most trajectories, during the second fire period, were directed to the East, mainly toward the Sea of Okhotsk and further. Additionally, one can see a high number of trajectories crossed the Arctic Circle and passed over the Arctic Ocean (Figure 12b). Overall, all trajectories' maps demonstrate the same pattern consistent with AI and CO spatial patterns over the period: transport of aerosol plumes originated during the second fire period in the study area was over distances of ~2000–5000 km in the northern, western and southern directions, and over ~5000–7000 km in the eastern direction.

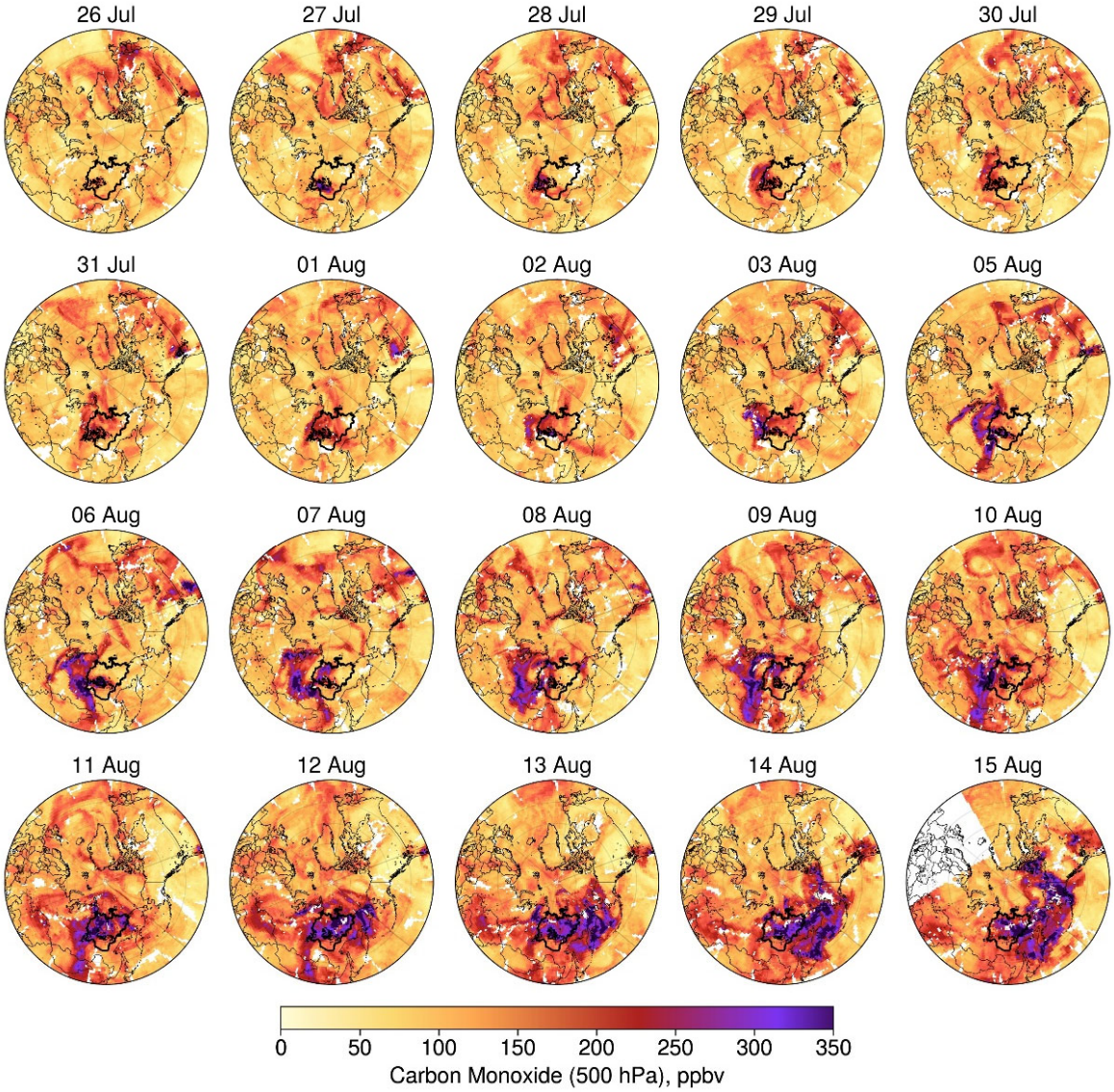

Figure 11. Spatial distribution of AIRS carbon monoxide concentration at 500 hPa during the second period of wildfire intensification in the study region (26 July–15 August). The bold solid line indicates Yakutia administrative boundary, black dots—MODIS hotspots.

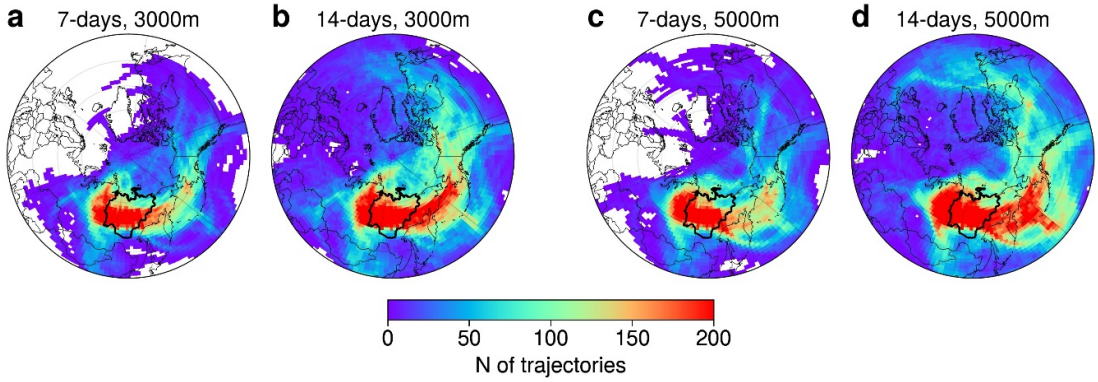

Figure 12. The number of HYSPLIT forward trajectories from 26 July to 15 August originated from 36 starting points evenly spaced over the study region (1.4° × 6° lat/lon). Trajectories forward runtime and starting altitudes are: (**a**) 7 days, 3000 m; (**b**) 14 days, 3000 m; (**c**) 7 days, 5000 m; (**d**) 14 days, 5000 m. The bold solid line indicates Yakutia's administrative boundary.

4. Discussion

Wildfires in Siberia are the major source of atmospheric aerosols which significantly affect the optical properties of the atmosphere during the summer [6,10,53,58–63]. The unprecedented wildfires in Yakutia in 2021 caused severe air pollution over a large territory, including Siberia's major population centers and the Arctic [64]. Record PM 2.5 emissions in Russia in 2021 were mostly caused by the forest fires in Yakutia and amounted to 8 Mt which is 78% higher than the average level [65].

There are a number of studies that show that the emergence of catastrophic wildfires in the boreal region is closely tied to atmospheric circulation patterns, which are a major driver of surface weather variability [22,27,28,66–69]. As was reported in the recent study by Hayasaka [26] and also shown in the present paper, the intensification of wildfires during the second fire period in August 2021 in Yakutia was associated with persistent high-pressure systems characterized by high Z500 and SLP anomalies that lasted from the end of July until 8 August, promoting favorable conditions for wildfires. Under global warming, it is expected that the frequency of weather events that promote such extreme conditions will increase [18–20,70,71].

High altitudes (9–11 km) aerosol layers observed by CALIOP in August 2021 are a phenomenon associated with the formation of deep pyrocumulative cumulonimbus clouds, which are formed by enhanced vertical convection promoted by intensive wildfires [72]. Smoke plumes from wildfires can reach high altitudes, in some cases comparable to the heights reached by volcanic emissions. Among recent examples, Cheremisin et al. [73] reported that biomass burning aerosols from Siberian wildfires in August 2019 were observed over Western Siberia at 10–17 km. Ohneiser et al. [74] reported a 10 km deep aerosol layer, presumably from Siberian wildfires, observed over the Arctic Ocean in 2019 at heights from 7 to 18 km. Ohneiser et al. [75] reported that smoke from extreme Australian bushfires in 2020 was observable up to heights of 30 km.

The long-range transport from midlatitude anthropogenic and biomass burning emissions is the main contributor to pollution in the Arctic [12–14]. With the increasing number of wildfires in the Siberian Arctic in the recent decade [76], one can expect a corresponding increase in transport of BC emissions to the Arctic where they may contribute to the acceleration of Arctic warming through the heating of the atmosphere and promoting the melting of snow and ice cover [9,14].

The present study has several shortcomings. Air temperature and precipitation are common meteorological parameters that provide a basic characteristic of weather conditions during a fire season. However, to reveal more insights into the relationship between weather conditions and wildfires in the region, the consideration of additional parameters is needed (water vapor deficit, drought indices, etc.). Daily and monthly values of precipitation were obtained from GPCC «first guess» products, which may be less accurate than «full data» products, which were unavailable at the time of preparation of this paper. MODIS observations over the study region are affected by the cloud cover, which may lead to a lower number of HS or inaccuracies in the daily mean AOD due to a limited number of cloud-free observations during a day. Most of the differences between MODIS-based and AERONET AOD should be attributed to the fact that satellite measurements are averaged over the study area while AERONET provides ground-based estimates at a single point. CALIOP is a nadir-pointing instrument with limited spatial coverage and a 16-day revisit cycle, which potentially may result in missed high-altitude aerosol layers over the study region.

5. Conclusions

In this study, we used satellite and ground-based observations along with reanalysis data to analyze the extreme fire season of 2021 in Yakutia and its impact on air pollution. The main findings of our study can be summarized as follows:

(1) The 2021 fire season in Yakutia was unprecedented in nearly four decades of satellite observations of wildfires in the region. The total number of hotspots in 2021 amounted

to ~150,000, which is almost twice as much as the previous record year (2020). One of the main features of the 2021 fire season is the period of extensive growth of the number of HS, which occurred from 24 July to 12 August. During this 20-day period, the total number of HS in the study region almost tripled from 49,000 to 140,000.

(2) High fire danger during the 2021 fire season was promoted by positive anomalies in monthly air temperature (August) and negative anomalies in monthly precipitation (May–July). August of 2021 in central Yakutia was the second most hot August (14.9 °C) during a 43-year NCEP-DOE Reanalysis record (1979–2021), second only to August of 2017 (15.0 °C) and followed by August 2002 (14.8 °C).

(3) Intensification of wildfires during the second fire period in August 2021 in Yakutia was associated with persistent high-pressure systems characterized by high Z500 and SLP anomalies, promoting dry weather conditions in the region by blocking the transport of moist air masses from the western part of Russia. Low wind speeds, observed in the center of a high-pressure system, led to the accumulation of wildfire emissions in the atmosphere, which resulted in heavy air pollution by smoke particles in the region.

(4) Monthly mean AOD values during July 2021 were 0.66 (DTDB), 0.82 (MAIAC), and 1.37 (AERONET) which were 7.8, 14.9, and 18.7 times higher than the respective values from 2007. August AOD was slightly lower primarily due to rainfalls in the middle of the month: 0.47 (DTDB), 0.64 (MAIAC), and 0.9 (AERONET), which exceed 2007 values by a factor of 6.3, 11.9, and 9.9, respectively.

(5) According to CALIOP observations, the seasonal pattern of aerosol OF over the study region during 2021 has two distinctive peaks—in winter and summer, contrary to 2007, where only the winter peak is clearly visible in all aerosol types. In August 2021, CALIOP observations revealed an increased abundance of smoke aerosols in the troposphere over the study region including several high-altitude layers with heights of up to 11 km.

(6) Smoke plumes originated from the study area during the second fire period and characterized by high AI and CO values were transported over long distances reaching the Ural Mountains in the west, Mongolia in the south, the North Pole in the north, and Alaska in the east, traveling the distances of ~2000–7000 km. Maximum spatial extent of the smoke plumes reached ~10–12 mln. km^2.

Author Contributions: Conceptualization, O.T. and V.S.; methodology, O.T.; formal analysis, O.T. and V.S.; investigation, O.T. and V.S.; data curation, O.T.; writing—original draft preparation, O.T.; writing—review and editing, O.T. and V.S.; visualization, O.T.; supervision, V.S. All authors have read and agreed to the published version of the manuscript.

Funding: This work was supported by the Ministry of Science and Higher Education of the Russian Federation and Siberian Branch of the Russian Academy of Sciences (No. 122011700172-2); the Academy of Sciences of the Republic of Sakha (Yakutia) (No. 8830, «Operational monitoring and assessment of the consequences of forest fires in Yakutia based on remote sensing data. Stage 1»).

Data Availability Statement: MODIS active fire data were obtained from The Fire Information for Resource Management System (FIRMS, https://firms.modaps.eosdis.nasa.gov/, accessed on 20 June 2022). MODIS AOD, OMPS-NM AI and AIRS CO products were obtained from NASA's Earth Observing System Data and Information System (EOSDIS, https://www.earthdata.nasa.gov/, accessed on 10 June 2022). AERONET data was obtained from the AERONET website (https://aeronet.gsfc.nasa.gov/, accessed on 19 July 2022). CALIOP data were obtained from NASA Atmospheric Science Data Center (ASDC, https://asdc.larc.nasa.gov/, accessed on 27 April 2022). NCEP–DOE II Reanalysis data were obtained from NOAA PSL (https://psl.noaa.gov/data/gridded/data.ncep.reanalysis2.html, accessed on 21 March 2022). GPCC precipitation products were obtained from the Global Precipitation Climatology Centre (https://opendata.dwd.de/climate_environment/GPCC/html/download_gate.html, accessed on 21 March 2022). All other data presented in this study are available from the corresponding author, upon reasonable request.

Acknowledgments: The authors want to thank Ludmila Akimova and Vladislav Petrov for providing the photos from the towns of Viluisk and Nyurba.

Conflicts of Interest: The authors declare no conflict of interest.

References

1. Conard, S.G.; Ivanova, G.A. Wildfire in Russian Boreal Forests—Potential Impacts of Fire Regime Characteristics on Emissions and Global Carbon Balance Estimates. *Environ. Pollut.* **1997**, *98*, 305–313. [CrossRef]
2. Archibald, S.; Lehmann, C.E.R.; Belcher, C.M.; Bond, W.J.; Bradstock, R.A.; Daniau, A.-L.; Dexter, K.G.; Forrestel, E.J.; Greve, M.; He, T.; et al. Biological and Geophysical Feedbacks with Fire in the Earth System. *Environ. Res. Lett.* **2018**, *13*, 033003. [CrossRef]
3. Kharuk, V.I.; Ponomarev, E.I.; Ivanova, G.A.; Dvinskaya, M.L.; Coogan, S.C.P.; Flannigan, M.D. Wildfires in the Siberian Taiga. *Ambio* **2021**. [CrossRef]
4. Veraverbeke, S.; Delcourt, C.J.F.; Kukavskaya, E.; Mack, M.; Walker, X.; Hessilt, T.; Rogers, B.; Scholten, R.C. Direct and Longer-Term Carbon Emissions from Arctic-Boreal Fires: A Short Review of Recent Advances. *Curr. Opin. Environ. Sci. Health* **2021**, *23*, 100277. [CrossRef]
5. Shaposhnikov, D.; Revich, B.; Bellander, T.; Bedada, G.B.; Bottai, M.; Kharkova, T.; Kvasha, E.; Lezina, E.; Lind, T.; Semutnikova, E.; et al. Mortality Related to Air Pollution with the Moscow Heat Wave and Wildfire of 2010. *Epidemiology* **2014**, *25*, 359–364. [CrossRef]
6. Antokhin, P.N.; Arshinova, V.G.; Arshinov, M.Y.; Belan, B.D.; Belan, S.B.; Davydov, D.K.; Ivlev, G.A.; Fofonov, A.V.; Kozlov, A.V.; Paris, J.-D.; et al. Distribution of Trace Gases and Aerosols in the Troposphere Over Siberia During Wildfires of Summer 2012. *J. Geophys. Res. Atmos.* **2018**, *123*, 2285–2297. [CrossRef]
7. Bondur, V.G.; Mokhov, I.I.; Voronova, O.S.; Sitnov, S.A. Satellite Monitoring of Siberian Wildfires and Their Effects: Features of 2019 Anomalies and Trends of 20-Year Changes. *Dokl. Earth Sc.* **2020**, *492*, 370–375. [CrossRef]
8. Stocker, M.; Ladstädter, F.; Steiner, A.K. Observing the Climate Impact of Large Wildfires on Stratospheric Temperature. *Sci. Rep.* **2021**, *11*, 22994. [CrossRef]
9. Evans, M.; Kholod, N.; Kuklinski, T.; Denysenko, A.; Smith, S.J.; Staniszewski, A.; Hao, W.M.; Liu, L.; Bond, T.C. Black Carbon Emissions in Russia: A Critical Review. *Atmos. Environ.* **2017**, *163*, 9–21. [CrossRef]
10. Tomshin, O.A.; Solovyev, V.S. The Impact of Large-Scale Forest Fires on Atmospheric Aerosol Characteristics. *Int. J. Remote Sens.* **2014**, *35*, 5742–5749.
11. Bondur, V.G.; Gordo, K.A.; Kladov, V.L. Spacetime Distributions of Wildfire Areas and Emissions of Carbon-Containing Gases and Aerosols in Northern Eurasia According to Satellite-Monitoring Data. *Izv. Atmos. Ocean. Phys.* **2017**, *53*, 859–874. [CrossRef]
12. Marelle, L.; Raut, J.-C.; Law, K.S.; Duclaux, O. Current and Future Arctic Aerosols and Ozone From Remote Emissions and Emerging Local Sources—Modeled Source Contributions and Radiative Effects. *J. Geophys. Res. Atmos.* **2018**, *123*. [CrossRef]
13. Sakerin, S.M.; Kabanov, D.M.; Kopeikin, V.M.; Kruglinsky, I.A.; Novigatsky, A.N.; Pol'kin, V.V.; Shevchenko, V.P.; Turchinovich, Y.S. Spatial Distribution of Black Carbon Concentrations in the Atmosphere of the North Atlantic and the European Sector of the Arctic Ocean. *Atmosphere* **2021**, *12*, 949. [CrossRef]
14. Matsui, H.; Mori, T.; Ohata, S.; Moteki, N.; Oshima, N.; Goto-Azuma, K.; Koike, M.; Kondo, Y. Contrasting Source Contributions of Arctic Black Carbon to Atmospheric Concentrations, Deposition Flux, and Atmospheric and Snow Radiative Effects. *Atmos. Chem. Phys.* **2022**, *22*, 8989–9009. [CrossRef]
15. Minsley, B.J.; Pastick, N.J.; Wylie, B.K.; Brown, D.R.N.; Andy Kass, M. Evidence for Nonuniform Permafrost Degradation after Fire in Boreal Landscapes. *J. Geophys. Res. Earth Surf.* **2016**, *121*, 320–335. [CrossRef]
16. Runge, A.; Nitze, I.; Grosse, G. Remote Sensing Annual Dynamics of Rapid Permafrost Thaw Disturbances with LandTrendr. *Remote Sens. Environ.* **2022**, *268*, 112752. [CrossRef]
17. Chylek, P.; Folland, C.; Klett, J.D.; Wang, M.; Hengartner, N.; Lesins, G.; Dubey, M.K. Annual Mean Arctic Amplification 1970–2020: Observed and Simulated by CMIP6 Climate Models. *Geophys. Res. Lett.* **2022**, *49*. [CrossRef]
18. Flannigan, M.; Cantin, A.S.; de Groot, W.J.; Wotton, M.; Newbery, A.; Gowman, L.M. Global Wildland Fire Season Severity in the 21st Century. *For. Ecol. Manag.* **2013**, *294*, 54–61. [CrossRef]
19. de Groot, W.J.; Flannigan, M.D.; Cantin, A.S. Climate Change Impacts on Future Boreal Fire Regimes. *For. Ecol. Manag.* **2013**, *294*, 35–44. [CrossRef]
20. Jones, M.W.; Abatzoglou, J.T.; Veraverbeke, S.; Andela, N.; Lasslop, G.; Forkel, M.; Smith, A.J.P.; Burton, C.; Betts, R.A.; van der Werf, G.R.; et al. Global and Regional Trends and Drivers of Fire Under Climate Change. *Rev. Geophys.* **2022**, *60*. [CrossRef]
21. Tomshin, O.; Solovyev, V. Spatio-Temporal Patterns of Wildfires in Siberia during 2001–2020. *Geocarto Int.* **2021**, 1–19. [CrossRef]
22. Mokhov, I.I.; Bondur, V.G.; Sitnov, S.A.; Voronova, O.S. Satellite Monitoring of Wildfires and Emissions into the Atmosphere of Combustion Products in Russia: Relation to Atmospheric Blockings. *Dokl. Earth Sc.* **2020**, *495*, 921–924. [CrossRef]
23. Sitnov, S.A.; Mokhov, I.I.; Likhosherstova, A.A. Exploring Large-Scale Black-carbon Air Pollution over Northern Eurasia in Summer 2016 Using MERRA-2 Reanalysis Data. *Atmos. Res.* **2020**, *235*, 104763. [CrossRef]
24. Hayasaka, H.; Tanaka, H.L.; Bieniek, P.A. Synoptic-Scale Fire Weather Conditions in Alaska. *Polar Sci.* **2016**, *10*, 217–226. [CrossRef]

25. Hayasaka, H.; Yamazaki, K.; Naito, D. Weather Conditions and Warm Air Masses during Active Fire-Periods in Boreal Forests. *Polar Sci.* **2019**, *22*, 100472. [CrossRef]
26. Hayasaka, H. Rare and Extreme Wildland Fire in Sakha in 2021. *Atmosphere* **2021**, *12*, 1572. [CrossRef]
27. Jain, P.; Flannigan, M. The Relationship between the Polar Jet Stream and Extreme Wildfire Events in North America. *J. Clim.* **2021**, 1–59. [CrossRef]
28. Sharma, A.R.; Jain, P.; Abatzoglou, J.T.; Flannigan, M. Persistent Positive Anomalies in Geopotential Heights Promote Wildfires in Western North America. *J. Clim.* **2022**, 1–41. [CrossRef]
29. Zhao, Z.; Lin, Z.; Li, F.; Rogers, B.M. Influence of Atmospheric Teleconnections on Interannual Variability of Arctic-Boreal Fires. *Sci. Total Environ.* **2022**, *838*, 156550. [CrossRef] [PubMed]
30. Tomshin, O.; Solovyev, V. Generating a Long-Term Data Series of Burned Area in Eastern Siberia Using LTDR Data (1984–2016). *Remote Sens. Lett.* **2019**, *10*, 1008–1017. [CrossRef]
31. Ponomarev, E.; Zabrodin, A.; Ponomareva, T. Classification of Fire Damage to Boreal Forests of Siberia in 2021 Based on the DNBR Index. *Fire* **2022**, *5*, 19. [CrossRef]
32. Krylov, A.; McCarty, J.L.; Potapov, P.; Loboda, T.; Tyukavina, A.; Turubanova, S.; Hansen, M.C. Remote Sensing Estimates of Stand-Replacement Fires in Russia, 2002–2011. *Environ. Res. Lett.* **2014**, *9*, 105007. [CrossRef]
33. Bartalev, S.A.; Stytsenko, F.V. Assessment of Forest-Stand Destruction by Fires Based on Remote-Sensing Data on the Seasonal Distribution of Burned Areas. *Contemp. Probl. Ecol.* **2021**, *14*, 711–716. [CrossRef]
34. Ponomarev, E.; Yakimov, N.; Ponomareva, T.; Yakubailik, O.; Conard, S.G. Current Trend of Carbon Emissions from Wildfires in Siberia. *Atmosphere* **2021**, *12*, 559. [CrossRef]
35. Gorokhov, A.N.; Fedorov, A.N. Current Trends in Climate Change in Yakutia. *Geogr. Nat. Resour.* **2018**, *39*, 153–161. [CrossRef]
36. *The Far North*; Troeva, E.I.; Isaev, A.P.; Cherosov, M.M.; Karpov, N.S. (Eds.) Plant and Vegetation; Springer: Dordrecht, Netherlands, 2010; Volume 3, ISBN 978-90-481-3773-2.
37. Xu, W.; Scholten, R.C.; Hessilt, T.D.; Liu, Y.; Veraverbeke, S. Overwintering Fires Rising in Eastern Siberia. *Environ. Res. Lett.* **2022**, *17*, 045005. [CrossRef]
38. Giglio, L.; Schroeder, W.; Justice, C.O. The Collection 6 MODIS Active Fire Detection Algorithm and Fire Products. *Remote Sens. Environ.* **2016**, *178*, 31–41. [CrossRef] [PubMed]
39. Schroeder, W.; Oliva, P.; Giglio, L.; Csiszar, I.A. The New VIIRS 375 m Active Fire Detection Data Product: Algorithm Description and Initial Assessment. *Remote Sens. Environ.* **2014**, *143*, 85–96. [CrossRef]
40. Anejionu, O.C.D.; Blackburn, G.A.; Whyatt, J.D. Detecting Gas Flares and Estimating Flaring Volumes at Individual Flow Stations Using MODIS Data. *Remote Sens. Environ.* **2015**, *158*, 81–94. [CrossRef]
41. Levy, R.C.; Mattoo, S.; Munchak, L.A.; Remer, L.A.; Sayer, A.M.; Patadia, F.; Hsu, N.C. The Collection 6 MODIS Aerosol Products over Land and Ocean. *Atmos. Meas. Tech.* **2013**, *6*, 2989–3034. [CrossRef]
42. Hsu, N.C.; Jeong, M.-J.; Bettenhausen, C.; Sayer, A.M.; Hansell, R.; Seftor, C.S.; Huang, J.; Tsay, S.-C. Enhanced Deep Blue Aerosol Retrieval Algorithm: The Second Generation: ENHANCED DEEP BLUE AEROSOL RETRIEVAL. *J. Geophys. Res. Atmos.* **2013**, *118*, 9296–9315. [CrossRef]
43. Lyapustin, A.; Wang, Y.; Korkin, S.; Huang, D. MODIS Collection 6 MAIAC Algorithm. *Atmos. Meas. Tech.* **2018**, *11*, 5741–5765. [CrossRef]
44. Holben, B.N.; Eck, T.F.; Slutsker, I.; Tanré, D.; Buis, J.P.; Setzer, A.; Vermote, E.; Reagan, J.A.; Kaufman, Y.J.; Nakajima, T.; et al. AERONET—A Federated Instrument Network and Data Archive for Aerosol Characterization. *Remote Sens. Environ.* **1998**, *66*, 1–16. [CrossRef]
45. Sinyuk, A.; Holben, B.N.; Eck, T.F.; Giles, D.M.; Slutsker, I.; Korkin, S.; Schafer, J.S.; Smirnov, A.; Sorokin, M.; Lyapustin, A. The AERONET Version 3 Aerosol Retrieval Algorithm, Associated Uncertainties and Comparisons to Version 2. *Atmos. Meas. Tech.* **2020**, *13*, 3375–3411. [CrossRef]
46. Winker, D.M.; Vaughan, M.A.; Omar, A.; Hu, Y.; Powell, K.A.; Liu, Z.; Hunt, W.H.; Young, S.A. Overview of the CALIPSO Mission and CALIOP Data Processing Algorithms. *J. Atmos. Ocean. Technol.* **2009**, *26*, 2310–2323. [CrossRef]
47. Kim, M.-H.; Omar, A.H.; Tackett, J.L.; Vaughan, M.A.; Winker, D.M.; Trepte, C.R.; Hu, Y.; Liu, Z.; Poole, L.R.; Pitts, M.C.; et al. The CALIPSO Version 4 Automated Aerosol Classification and Lidar Ratio Selection Algorithm. *Atmos. Meas. Tech.* **2018**, *11*, 6107–6135. [CrossRef]
48. Susskind, J.; Blaisdell, J.M.; Iredell, L. Improved Methodology for Surface and Atmospheric Soundings, Error Estimates, and Quality Control Procedures: The Atmospheric Infrared Sounder Science Team Version-6 Retrieval Algorithm. *J. Appl. Remote Sens.* **2014**, *8*, 084994. [CrossRef]
49. Kanamitsu, M.; Ebisuzaki, W.; Woollen, J.; Yang, S.-K.; Hnilo, J.J.; Fiorino, M.; Potter, G.L. NCEP–DOE AMIP-II Reanalysis (R-2). *Bull. Amer. Meteor. Soc.* **2002**, *83*, 1631–1644. [CrossRef]
50. Becker, A.; Finger, P.; Meyer-Christoffer, A.; Rudolf, B.; Schamm, K.; Schneider, U.; Ziese, M. A Description of the Global Land-Surface Precipitation Data Products of the Global Precipitation Climatology Centre with Sample Applications Including Centennial (Trend) Analysis from 1901–Present. *Earth Syst. Sci. Data* **2013**, *5*, 71–99. [CrossRef]
51. Schneider, U.; Becker, A.; Finger, P.; Meyer-Christoffer, A.; Ziese, M.; Rudolf, B. GPCC's New Land Surface Precipitation Climatology Based on Quality-Controlled in Situ Data and Its Role in Quantifying the Global Water Cycle. *Theor. Appl. Climatol.* **2014**, *115*, 15–40. [CrossRef]

52. Stein, A.F.; Draxler, R.R.; Rolph, G.D.; Stunder, B.J.B.; Cohen, M.D.; Ngan, F. NOAA's HYSPLIT Atmospheric Transport and Dispersion Modeling System. *Bull. Am. Meteorol. Soc.* **2015**, *96*, 2059–2077. [CrossRef]
53. Tomshin, O.A.; Solovyev, V.S. Features of Forest Fire Activity in Boreal Forests of the Permafrost Region of Eastern Siberia. *Sovr. Probl. DZZ Kosm.* **2018**, *15*, 261–271. [CrossRef]
54. Hayasaka, H. Recent Vegetation Fire Incidence in Russia. *Glob. Environ. Res.* **2011**, *15*, 5–13.
55. Levy, R.C.; Remer, L.A.; Dubovik, O. Global Aerosol Optical Properties and Application to Moderate Resolution Imaging Spectroradiometer Aerosol Retrieval over Land. *J. Geophys. Res.* **2007**, *112*, 2006JD007815. [CrossRef]
56. Lyapustin, A.; Korkin, S.; Wang, Y.; Quayle, B.; Laszlo, I. Discrimination of Biomass Burning Smoke and Clouds in MAIAC Algorithm. *Atmos. Chem. Phys.* **2012**, *12*, 9679–9686. [CrossRef]
57. Sakerin, S.M.; Andreev, S.Y.; Kabanov, D.M.; Nikolashkin, S.V.; Prakhov, A.N.; Radionov, V.F.; Turchinovich, Y.S.; Chernov, D.G.; Holben, B.N.; Smirnov, A.; et al. On Results of Studies of Atmospheric Aerosol Optical Depth in Arctic Regions. *Atmos. Ocean Opt.* **2014**, *27*, 517–528. [CrossRef]
58. Mikhailov, E.F.; Mironova, S.Y.; Makarova, M.V.; Vlasenko, S.S.; Ryshkevich, T.I.; Panov, A.V.; Andreae, M.O. Studying Seasonal Variations in Carbonaceous Aerosol Particles in the Atmosphere over Central Siberia. *Izv. Atmos. Ocean. Phys.* **2015**, *51*, 423–430. [CrossRef]
59. Panchenko, M.V.; Zhuravleva, T.B.; Kozlov, V.S.; Nasrtdinov, I.M.; Pol'kin, V.V.; Terpugova, S.A.; Chernov, D.G. Estimation of Aerosol Radiation Effects under Background and Smoke-Haze Atmospheric Conditions over Siberia from Empirical Data. *Russ. Meteorol. Hydrol.* **2016**, *41*, 104–111. [CrossRef]
60. Zhuravleva, T.B.; Kabanov, D.M.; Nasrtdinov, I.M.; Russkova, T.V.; Sakerin, S.M.; Smirnov, A.; Holben, B.N. Radiative Characteristics of Aerosol during Extreme Fire Event over Siberia in Summer 2012. *Atmos. Meas. Tech.* **2017**, *10*, 179–198. [CrossRef]
61. Konovalov, I.B.; Golovushkin, N.A.; Beekmann, M.; Andreae, M.O. Insights into the Aging of Biomass Burning Aerosol from Satellite Observations and 3D Atmospheric Modeling: Evolution of the Aerosol Optical Properties in Siberian Wildfire Plumes. *Atmos. Chem. Phys.* **2021**, *21*, 357–392. [CrossRef]
62. Taschilin, M.; Yakovleva, I.; Sakerin, S.; Zorkaltseva, O.; Tatarnikov, A.; Scheglova, E. Spatiotemporal Variations of Aerosol Optical Depth in the Atmosphere over Baikal Region Based on MODIS Data. *Atmosphere* **2021**, *12*, 1706. [CrossRef]
63. Zabukovec, A.; Ancellet, G.; Penner, I.E.; Arshinov, M.; Kozlov, V.; Pelon, J.; Paris, J.-D.; Kokhanenko, G.; Balin, Y.S.; Chernov, D.; et al. Characterization of Aerosol Sources and Optical Properties in Siberia Using Airborne and Spaceborne Observations. *Atmosphere* **2021**, *12*, 244. [CrossRef]
64. Efimova, N.V.; Rukavishnikov, V.S. Assessment of Smoke Pollution Caused by Wildfires in the Baikal Region (Russia). *Atmosphere* **2021**, *12*, 1542. [CrossRef]
65. Romanov, A.A.; Tamarovskaya, A.N.; Gusev, B.A.; Leonenko, E.V.; Vasiliev, A.S.; Krikunov, E.E. Catastrophic PM2.5 Emissions from Siberian Forest Fires: Impacting Factors Analysis. *Environ. Pollut.* **2022**, *306*, 119324. [CrossRef] [PubMed]
66. Gedalof, Z.; Peterson, D.L.; Mantua, N.J. Atmospheric, climatic, and ecological controls on extreme wildfire years in the Northwestern United States. *Ecol. Appl.* **2005**, *15*, 154–174. [CrossRef]
67. Macias Fauria, M.; Johnson, E.A. Large-Scale Climatic Patterns Control Large Lightning Fire Occurrence in Canada and Alaska Forest Regions: FOREST FIRES AND CLIMATE. *J. Geophys. Res.* **2006**, *111*. [CrossRef]
68. Hostetler, S.W.; Bartlein, P.J.; Alder, J.R. Atmospheric and Surface Climate Associated With 1986–2013 Wildfires in North America. *J. Geophys. Res. Biogeosci.* **2018**, *123*, 1588–1609. [CrossRef]
69. Hayasaka, H. Fire Weather Conditions in Boreal and Polar Regions in 2002–2021. *Atmosphere* **2022**, *13*, 1117. [CrossRef]
70. Flannigan, M.D.; Amiro, B.D.; Logan, K.A.; Stocks, B.J.; Wotton, B.M. Forest Fires and Climate Change in the 21ST Century. *Mitig Adapt. Strat. Glob Change* **2006**, *11*, 847–859. [CrossRef]
71. Jain, P.; Castellanos-Acuna, D.; Coogan, S.C.P.; Abatzoglou, J.T.; Flannigan, M.D. Observed Increases in Extreme Fire Weather Driven by Atmospheric Humidity and Temperature. *Nat. Clim. Chang.* **2021**. [CrossRef]
72. Fromm, M.; Lindsey, D.T.; Servranckx, R.; Yue, G.; Trickl, T.; Sica, R.; Doucet, P.; Godin-Beekmann, S. The Untold Story of Pyrocumulonimbus. *Bull. Amer. Meteor. Soc.* **2010**, *91*, 1193–1210. [CrossRef]
73. Cheremisin, A.A.; Marichev, V.N.; Bochkovskii, D.A.; Novikov, P.V.; Romanchenko, I.I. Stratospheric Aerosol of Siberian Forest Fires According to Lidar Observations in Tomsk in August 2019. *Atmos. Ocean Opt.* **2022**, *35*, 57–64. [CrossRef]
74. Ohneiser, K.; Ansmann, A.; Chudnovsky, A.; Engelmann, R.; Ritter, C.; Veselovskii, I.; Baars, H.; Gebauer, H.; Griesche, H.; Radenz, M.; et al. The Unexpected Smoke Layer in the High Arctic Winter Stratosphere during MOSAiC 2019–2020. *Atmos. Chem. Phys.* **2021**, *21*, 15783–15808. [CrossRef]
75. Ohneiser, K.; Ansmann, A.; Baars, H.; Seifert, P.; Barja, B.; Jimenez, C.; Radenz, M.; Teisseire, A.; Floutsi, A.; Haarig, M.; et al. Smoke of Extreme Australian Bushfires Observed in the Stratosphere over Punta Arenas, Chile, in January 2020: Optical Thickness, Lidar Ratios, and Depolarization Ratios at 355 and 532 Nm. *Atmos. Chem. Phys.* **2020**, *20*, 8003–8015. [CrossRef]
76. Kharuk, V.I.; Dvinskaya, M.L.; Im, S.T.; Golyukov, A.S.; Smith, K.T. Wildfires in the Siberian Arctic. *Fire* **2022**, *5*, 106. [CrossRef]